First-principles thermal conductivity of warm-dense deuterium plasmas for inertial confinement fusion applications

S. X. Hu (胡素兴),[1,*] L. A. Collins,[2] T. R. Boehly,[1] J. D. Kress,[2] V. N. Goncharov,[1] and S. Skupsky[1]
[1]*Laboratory for Laser Energetics, University of Rochester, Rochester, New York 14623, USA*
[2]*Theoretical Division, Los Alamos National Laboratory, Los Alamos, New Mexico 87545, USA*
(Received 11 December 2013; published 16 April 2014)

Thermal conductivity (κ) of both the ablator materials and deuterium-tritium (DT) fuel plays an important role in understanding and designing inertial confinement fusion (ICF) implosions. The extensively used Spitzer model for thermal conduction in ideal plasmas breaks down for high-density, low-temperature shells that are compressed by shocks and spherical convergence in imploding targets. A variety of thermal-conductivity models have been proposed for ICF hydrodynamic simulations of such coupled and degenerate plasmas. The accuracy of these κ models for DT plasmas has recently been tested against first-principles calculations using the quantum molecular-dynamics (QMD) method; although mainly for high densities ($\rho > 100$ g/cm^3), large discrepancies in κ have been identified for the peak-compression conditions in ICF. To cover the wide range of density-temperature conditions undergone by ICF imploding fuel shells, we have performed QMD calculations of κ for a variety of deuterium densities of $\rho = 1.0$ to 673.518 g/cm^3, at temperatures varying from $T = 5 \times 10^3$ K to $T = 8 \times 10^6$ K. The resulting $\kappa_{\rm QMD}$ of deuterium is fitted with a polynomial function of the coupling and degeneracy parameters Γ and θ, which can then be used in hydrodynamic simulation codes. Compared with the "hybrid" Spitzer-Lee-More model currently adopted in our hydrocode LILAC, the hydrosimulations using the fitted $\kappa_{\rm QMD}$ have shown up to ~20% variations in predicting target performance for different ICF implosions on OMEGA and direct-drive–ignition designs for the National Ignition Facility (NIF). The lower the adiabat of an imploding shell, the more variations in predicting target performance using $\kappa_{\rm QMD}$. Moreover, the use of $\kappa_{\rm QMD}$ also modifies the shock conditions and the density-temperature profiles of the imploding shell at early implosion stage, which predominantly affects the final target performance. This is in contrast to the previous speculation that $\kappa_{\rm QMD}$ changes mainly the inside ablation process during the hot-spot formation of an ICF implosion.

DOI: 10.1103/PhysRevE.89.043105 PACS number(s): 52.25.Fi, 65.20.De, 52.25.Kn, 52.27.Gr

I. INTRODUCTION

As a grand challenge to harvest the "ultimate" energy source in a controlled fashion, inertial confinement fusion (ICF) [1] has been actively pursued for decades using both indirect-drive [2,3] and direct-drive [4–6] configurations. Understanding and designing ICF capsule implosions rely on simulations using multiphysics, radiation-hydrodynamics codes, in which each piece of the physics models must be as accurate as possible. According to the ICF ignition criterion [7,8], the minimum laser energy required for ignition scales as

$$E_{\rm L}({\rm kJ}) \simeq 590\alpha^{1.9}\left(\frac{3\times10^7}{V_{\rm imp}}\right)^{6.6}\left(\frac{P_a}{100\ {\rm Mbar}}\right)^{-0.8}, \quad (1)$$

where the implosion velocity $V_{\rm imp}$ is in cm/s and the DT shell's adiabat α is conventionally defined as $\alpha = P/P_{\rm F}$, the ratio of plasma pressure to the Fermi-degeneracy pressure ($P_{\rm F}$). P_α is the ablation pressure in Mbar. This scaling law indicates that the lower the shell adiabat, the less energy needed for ignition. For lower-α implosions, however, the DT shell is in the regime in which strong coupling and degeneracy plasma effects are important and they need to be taken into account for accurate implosion modeling.

The determination of accurate plasma properties is very important for understanding low-adiabat ($\alpha \le 2$) ICF implosions. One of the examples is the precise knowledge of the static and dynamic properties of ICF target materials, including ablators and the deuterium-tritium (DT) fuel, under high-energy-density conditions. For instance, the equation-of-state (EOS) of the target materials determines how much compression can be attained under certain external pressures generated by x-ray and laser ablations [9]. Exactly for this reason, state-of-the-art EOS experiments and calculations have been performed for ICF-relevant materials [10–16] over the past few years. The theoretical approaches have employed first-principles methods such as the path-integral Monte Carlo (PIMC) [17], coupled electron-ion Monte Carlo (CEIMC) [18], and quantum molecular dynamics (QMD) [19] based on the finite-temperature density-functional theory. Besides the static EOS information, the dynamic transport properties of ICF-relevant materials are also in high demand for accurate ICF simulations, given that transport and optical properties (thermal and electrical conductivities) of DT and ablators cannot only affect the thermal conduction but also essentially determine the radiation transport in the imploding shell.

Soon after the introduction of the ICF concept [1] in 1972, there followed studies to determine the most-appropriate models for thermal conductivity for strongly coupled and degenerate plasmas in the high-density, low-temperature regime [20]. The Spitzer model [21] of thermal conductivity κ, formulated in the 1950s for ideal plasmas, breaks down in this regime, given that the Coulomb logarithm [22–26] for electron-ion collisions becomes negative. Brysk *et al.* [20] suggested in the 1970s that the Hubbard model [27] of degenerate plasma be "bridged" with the Spitzer model [21]. However, the analytical formula given in the Brysk paper [20] is only for the weak-coupling regime. In the 1980s,

*shu@lle.rochester.edu

 ©2014 American Physical Society

Lee and More [28] applied Krook's model to the Boltzmann equation and derived a set of transport coefficients including κ. Meanwhile, Ichimaru and colleagues [29] developed the so-called "Ichimaru model" of thermal conductivity for fully ionized plasmas, using the linear response theory. In addition, the average-atom model [30] and its improved versions have also been used to numerically calculate κ for materials interesting to ICF and astrophysics, such as the PURGATORIO package [31] and the SCAALP model [32] As a result of recent progress in the *first-principles* method of quantum molecular dynamics [33–37], these various thermal-conductivity models of hydrogen/DT have been tested with QMD calculations [38–43]. For ICF stagnation plasma conditions near peak compression, the pioneering QMD calculations by Recoules *et al.* [38] have shown orders-of-magnitude increase in κ for the coupled and degenerate regimes when compared with the extensively used Lee-More model for a corresponding deuterium density of $\rho_D \simeq 160$ g/cm^3.

These recent studies have motivated us to investigate how the more-accurate results of thermal conductivity κ derived from QMD calculations could affect the hydroprediction of ICF implosions. Apparently the κ change in the ablator materials [40] (CH, Be, or C) can enhance heat flowing into the cold shell from the hot coronal plasma. This may modify the mass ablation rate, thereby altering the implosion velocity. No wide range of density-temperature data exist, however, from QMD calculations of κ of ICF ablator materials. These effects on ICF target performance are left for future studies. Here we focus on how the QMD-calculated κ of fuel DT might affect ICF simulations. Recently, Lambert *et al.* [39] have extended their original QMD calculations of κ_{DT} for three different densities of $\rho_{DT} = 25$, 200, and 400 g/cm^3. They argued that the variation of κ_{DT} can change the thermodynamical path to ignition by modifying the inside ablation process at the boundary between the hot core and the dense cold shell. Under similar circumstances, Wang *et al.* [43] have also computed κ_{DT} for several other high-density points of $\rho_{DT} = 200$ to 600 g/cm^3, using the QMD simulation package ABINIT [44]. They briefly discussed the κ effects in hydrosimulations, solely based on their high-density QMD results.

As we have shown previously [45], the imploding DT shell undergoes a wide range of densities from $\rho_{DT} \simeq 1.0$ g/cm^3 at the shock transit stage and $\rho_{DT} \simeq 5.0$ to 10.0 g/cm^3 during in-flight shell acceleration, up to $\rho_{DT} \geq 300$ g/cm^3 at stagnation (i.e., at the peak compression). To cover all the relevant density points in ICF, we have performed QMD calculations of the thermal conductivity κ through the usual Kubo-Greenwood formulation [46], by spanning deuterium densities from $\rho \simeq 1.0$ g/cm^3 to $\rho \simeq 673.518$ g/cm^3 at temperatures varying from $T = 5000$ K to $T = 8\,000\,000$ K. We have compared the calculated κ_{QMD} with the following "hydrid" thermal-conductivity model currently used in our hydrocode LILAC [47]:

$$\kappa_{LILAC} = \frac{20(2/\pi)^{3/2}k_B^{7/2}T^{5/2}}{\sqrt{m_e}Z_{eff}e^4}\frac{0.095(Z_{eff}+0.24)}{1+0.24Z_{eff}} \times \frac{1}{[\ln\Lambda]_{LM}} f_{LM(\rho,T)}. \quad (2)$$

In this hybrid model of κ_{LILAC}, the Spitzer prefactor is used in combination with the replacement of the Spitzer Coulomb logarithm by that of Lee and More, $[\ln\Lambda]_{LM}$. In addition, the Lee-More degeneracy correction function $f_{LM}(\rho,T)$ has also been adopted in the following form:

$$f_{LM}(\rho,T) = 1 + \frac{3\pi^5}{51\,200}\left(\frac{T_F}{T}\right)^3\left[\frac{1+0.24Z_{eff}}{0.095(Z_{eff}+0.24)}\right]^2, \quad (3)$$

where $T_F = (\hbar^2/2m_ek_B)(3\pi^2n_e)^{2/3}$ is the Fermi temperature of the electrons in a fully ionized plasma, k_B is the Boltzmann constant, and m_e and n_e are the mass and number density of electrons. The effective charge of ions is defined as $Z_{eff} = \langle Z^2\rangle/\langle Z\rangle$ averaging over the species ($Z_{eff} = 1$ for fully ionized DT plasmas). In general, our QMD results showed a factor of 3 to 10 enhancement in κ_{QMD} over κ_{LILAC} within the ICF-relevant density-temperature ranges.

In contrast to the various thermal-conductivity models, the global κ_{QMD} formula we figured out through systematic QMD simulations cover the overall coupling and degeneracy parameter regimes important to ICF. Such a global behavior of thermal conductivity of deuterium plasmas, obtained from fitting to QMD calculations, is essential to be applied for ICF simulations. To test the effects of κ_{QMD} on ICF implosions, we have fitted the calculated κ_{QMD} with a fifth-order polynomial function of the coupling parameter $\Gamma = 1/(r_Sk_BT)$ and the degeneracy parameter $\theta = T/T_F$. The Wigner-Seitz radius r_S is related to the electron number density $n_e = 3/(4\pi r_S^3)$. The fitted formula of κ_{QMD} is then applied in our radiation hydrodynamics code LILAC to simulate a variety of cryogenic DT implosions on OMEGA as well as direct-drive designs on the NIF. Comparing with the standard hydrosimulations using κ_{LILAC}, we found up to ~20% variations in the target-performance predictions using the more-accurate κ_{QMD}. The lower the adiabat of imploding shells, the stronger the coupling and degeneracy effects in κ_{QMD}.

The paper is organized as follows: The QMD method is described briefly in Sec. II, in which other methods and experiments on deuterium plasma properties are examined. In Sec. III, the calculated κ_{QMD} of deuterium for a wide range of density and temperature points is presented and compared with κ_{LILAC}. In Sec. IV, the κ_{QMD} effects on the ICF implosion dynamics are discussed in detail. The paper is summarized in Sec. V.

II. THE QUANTUM MOLECULAR-DYNAMICS METHOD

We have used the QMD method for simulating warm dense deuterium plasmas. Since the QMD procedures have been well-documented elsewhere [34,48–50], we present only a brief description of its basics. The Vienna *ab initio* simulation package (VASP) [51,52] has been employed within the isokinetic ensemble (*NVT* constant). VASP is based on the finite-temperature density-functional theory (FTDFT). To be specific, the electrons are treated quantum mechanically by plane-wave FTDFT calculations using the Perdew-Burke-Ernzerhof (PBE) exchange-correlation functional [53] under the generalized gradient approximation (GGA). The electron-ion interaction was modeled by either a projector argumented wave (PAW) pseudopotential or the pure Coulombic potential.

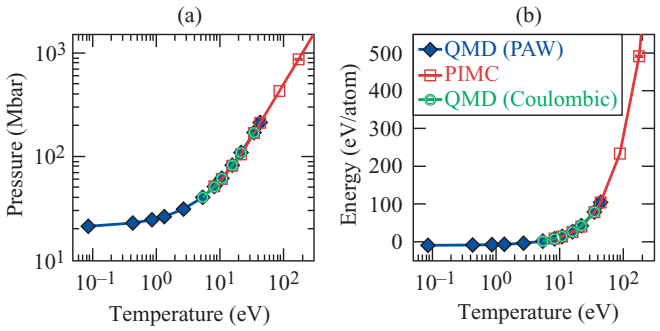

FIG. 1. (Color online) The equation-of-state comparison between QMD and PIMC calculations for deuterium density at $\rho = 5.388$ g/cm^3: (a) Pressure versus temperature and (b) internal energy versus temperature.

The system assumed to be in local thermodynamical equilibrium with equal electron and ion temperatures ($T_e = T_i$). The ion temperature kept constant by simple velocity scaling.

A periodically replicated cubic cell was used with equal numbers of electrons and deuterium ions. The plasma density and the number of D atoms determined the volume of the cell. For the present simulations of densities below $\rho_D = 15.709$ g/cm^3, we employed 128 atoms and the PAW pseudopotential. For high densities ($\rho_D \geq 15.709$ g/cm^3, a varying number of atoms ($N = 216$ to 1000) were used, incorporated with the pure Coulombic potential [54]. For each molecular dynamics (MD) step, a set of electronic state functions for each k point was self-consistently determined for an ionic configuration. Then, the ions were moved classically with a velocity Verlet algorithm, according to the combined ionic force and the electronic force. Repeating the two steps propagated the system in time, resulting in a set of self-consistent ion trajectories and electronic state functions. These trajectories provide a consistent set of static, dynamical, and optical properties of the deuterium plasmas.

All of our QMD calculations employed only Γ-point ($\mathbf{k} = 0$) sampling of the first Brillouin zone in the cubic cell; such a sampling has been shown to produce properties of sufficient accuracy in this regime [39,43]. When we increased the k-point sets to an $4 \times 4 \times 4$ Monkhorst-Pack grid, the results vary only ~2%. For low-density points, the tight PAW pseudopotential was used with a maximum energy cutoff of $E_{max} = 700$ eV to avoid core overlap. The Coulombic potential for high-density points had a cutoff energy varying from $E_{max} = 1000$ eV to $E_{max} = 8000$ eV. A large number of energy bands (up to $N_b = 3500$) were included to ensure the lowest population down to a level of 10^{-5}. To benchmark our current QMD calculations, we first compare the EOS results with previous PIMC calculations [11] for a deuterium density of $\rho_D = 5.388$ g/cm^3. Both the QMD calculation using PAW pseudopotential and the PIMC simulation used 128 atoms in the cell. The total pressure is a sum of the electronic pressure (averaging over the MD times) and the classical ionic pressure; the internal energy is referenced to the ground-state energy ($E_0 = -15.886$ eV) of the D_2 molecule. The EOS results shown in Fig. 1 demonstrated the excellent agreement within the overlapping temperature range where both methods are valid. In addition, we have also performed convergence tests of QMD calculations by using the Coulombic potential and more atoms ($N = 343$) for this density. The results are plotted by green open circles in Fig. 1, which are almost identical to the PAW calculations.

To calculate the electron thermal conductivity of a plasma, we consider the linear response of the plasma to an electric field $\mathbf{E}$ and a temperature gradient ∇T, which induce the electric current $\mathbf{j}_e$ and the heat flux $\mathbf{j}_q$,

$$\mathbf{j}_e = \left(eL_{11}\mathbf{E} - \frac{L_{12}\nabla T}{T} \right) \Big/ e, \tag{4}$$

$$\mathbf{j}_q = \left(eL_{21}\mathbf{E} - \frac{L_{22}\nabla T}{T} \right) \Big/ e, \tag{5}$$

For plasmas having no electric current ($\mathbf{j}_e = 0$), the above equations in combination with the definition of $\boldsymbol{j}_q = -\kappa \nabla T$ give the thermal conductivity

$$\kappa = \frac{1}{T}\left(L_{22} - \frac{L_{12}^2}{L_{11}} \right), \tag{6}$$

with the Onsager coefficients given by L_{ij}. In the absence of temperature gradient ($\nabla T = 0$), Eq. (4) reduces to the Ohm's law with the electrical conductivity of $\sigma = L_{11}$. The calculation of frequency-dependent Onsager coefficients can be done using the Kubo-Greenwood formalism [46]:

$$L_{ij}(\omega) = \frac{2\pi(-e)^{4-i-j}}{3Vm_e^2\omega} \sum_{m,n} F_{mn}|D_{mn}|^2 \times \left(\frac{E_m + E_n}{2} - H \right)^{i+j-2} \delta(E_m - E_n - \hbar\omega), \tag{7}$$

where V is the atomic volume, E_m (E_n) is the energy of the mth (nth) state, and H is the enthalpy (per atom) of the system. The quantity of F_{mn} is the difference between the Fermi-Dirac distributions for the involved states m and n at temperature T. The velocity dipole matrix elements D_{mn} can be computed from the VASP wave functions. In practical calculations, the δ function in the above equation is approximated by a Gaussian function of width ΔE (=0.1 to 0.5 eV). In addition, $L_{ij} = L_{ij}(0)$ is used in Eq. (6). The resulting κ was averaged over at least ten snapshots of uncorrelated configurations along the MD trajectories. The determination of κ required, for convergence, a much larger number of energy bands (~2–3×) than for the MD simulation.

Since no direct measurements exist for the thermal conductivity in deuterium plasmas, we compared our QMD calculations to a related optical property, the reflectivity, which has been determined along the principal Hugoniot in shock-timing experiments [55–58] using the velocity interferometer system for any reflector (VISAR). The reflectivity is determined by

$$R(\omega) = \frac{[1 - n(\omega)]^2 + k(\omega)^2}{[1 + n(\omega)]^2 + k(\omega)^2}, \tag{8}$$

with the real and imaginary parts of refraction indices $[n(\omega),k(\omega)]$ that can be computed from the dielectric function of $\varepsilon(\omega) = \varepsilon_1(\omega) + i\varepsilon_2(\omega)$. The dielectric functions are obtained from the real electric conductivity $\sigma_1(\omega) = L_{11}(\omega)$ and its imaginary part $\sigma_2(\omega)$ determined by a principal-value integral of $\sigma_1(\omega)$. In Fig. 2 the calculated reflectivities of

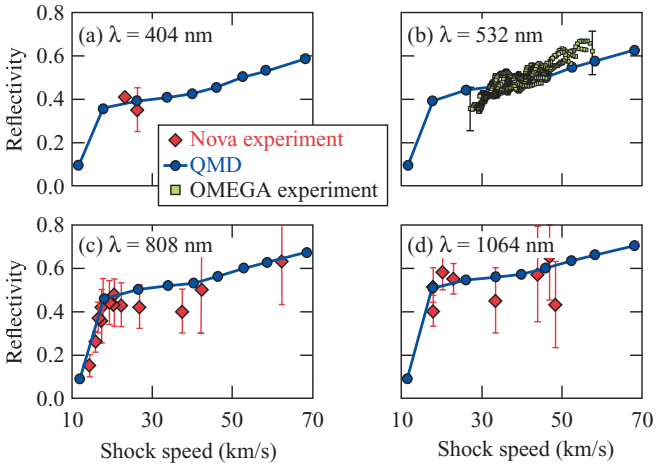

FIG. 2. (Color online) The QMD-calculated reflectivity of deuterium shock as a function of shock speed along the principal Hugoniot, which is compared to both the previous Nova measurement [55] and the recent OMEGA experiment for different VISAR wavelengths: (a) $\lambda = 404$ nm, (b) $\lambda = 532$ nm, (c) $\lambda = 808$ nm, and (d) $\lambda = 1064$ nm.

deuterium as a function of shock speed for different VISAR wavelengths are compared with both Nova [55] and recent OMEGA measurements along the principal Hugoniot. The OMEGA experiments were taken from a decayed shock in deuterium for many shots. This experimental confirmation together with agreement with other first-principle results [34,50,59] lends credence to the L_{11} coefficients produced in this study and in turn to the other similarly calculated Onsager coefficients that determine κ.

III. THERMAL CONDUCTIVITY OF DEUTERIUM FOR A WIDE RANGE OF DENSITIES AND TEMPERATURES

The QMD calculations of deuterium thermal conductivity have been performed for a wide range of densities [$\rho = 1.0$ to 673.518 g/cm^3], at temperatures varying from $T = 5 \times 10^3$ K to $T = 8 \times 10^6$ K. For each density point, the $\kappa_{\rm QMD}$ calculations have been performed to the highest temperature approaching $T \simeq T_{\rm F}$. Tabulated results of $\kappa_{\rm QMD}$ are found in the Supplementary Material [60]. To test the effects of $\kappa_{\rm QMD}$ on ICF implosions, we have fitted these results to the following function (in a similar format of $\kappa_{\rm LILAC}$):

$$\kappa_{\rm QMD} = \frac{20(2/\pi)^{3/2} k_{\rm B}^{7/2} T^{5/2}}{\sqrt{m_{\rm e}} Z_{\rm eff} e^4} \frac{0.095(Z_{\rm eff} + 0.24)}{1 + 0.24 Z_{\rm eff}} \frac{1}{(\ln\Lambda)_{\rm QMD}}, \quad (9)$$

TABLE I. The fitting parameters for $(\ln\Lambda)_{\rm QMD}$.

i	α_i	β_i
0	-0.74014809257279	
1	-0.18145905042211	$+0.861554200945883$
2	$+6.39644338111 \times 10^{-4}$	-0.105703692158405
3	$+1.47954277819 \times 10^{-3}$	$-6.757828681522 \times 10^{-3}$
4	$-1.23361568162 \times 10^{-4}$	$-1.690070651236 \times 10^{-4}$
5	$-2.58107191013 \times 10^{-5}$	$+3.492008487199 \times 10^{-4}$

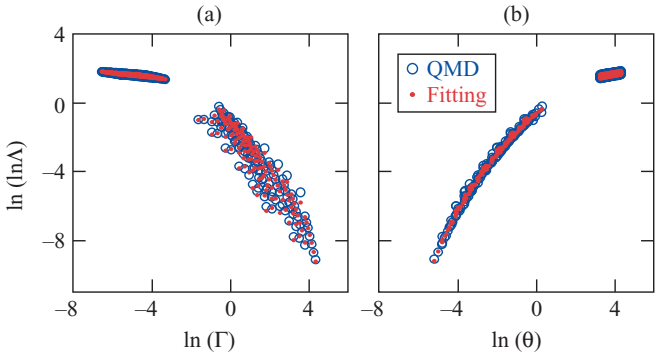

FIG. 3. (Color online) The generalized Coulomb logarithm, derived from QMD-calculated thermal conductivities for different densities and temperatures, is fitted with the polynomial function [Eq. (10)] of the coupling parameter (Γ) and the degeneracy parameter (θ). The values of $\ln\Lambda$ at high temperatures [i.e., $\ln(\ln\Lambda) > 0$] are converged to the standard LILAC ones.

with the same Spitzer prefactor as used in $\kappa_{\rm LILAC}$ and $Z_{\rm eff} = 1$. The generalized QMD Coulomb logarithm has the following form:

$$(\ln\Lambda)_{\rm QMD} = \exp\left\{\alpha_0 + \sum_{i=1}^{5} [\alpha_i (\ln\Gamma)^i + \beta_i (\ln\theta)^i]\right\}. \quad (10)$$

This fifth-order polynomial function of coupling and degeneracy parameters (Γ,θ) has been fitted with the $\kappa_{\rm QMD}$ data using multivariable least-square fitting. To make $\kappa_{\rm QMD}$ converge to $\kappa_{\rm LILAC}$ at the ideal plasma conditions ($\Gamma \ll 1$ and $\theta \gg 1$), we have added those high-temperature points of $\kappa_{\rm LILAC}$ into the data set for the global fitting. The resulting fitting parameters are listed in Table I.

The fit results of $(\ln\Lambda)_{\rm QMD}$ are plotted in Figs. 3(a) and 3(b) as a function of $\ln(\Gamma)$and $\ln(\theta)$, respectively. Overall, the global fitting with the above parameters gives only a small error of ~5%.

Comparisons of $\kappa_{\rm QMD}$ with $\kappa_{\rm LILAC}$ are plotted in Figs. 4 and 5 for deuterium densities of $\rho = 2.453$, 10.0, 43.105, and 199.561 g/cm^3. The green dashed lines represent the thermal

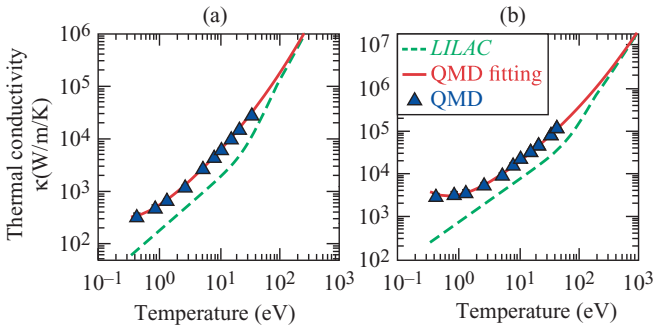

FIG. 4. (Color online) The thermal conductivities from first-principles QMD calculations, the QMD-fitting formula [Eq. (10)], and the hybrid model used in LILAC are plotted as a function of temperature for different deuterium densities of (a) $\rho = 2.453$ g/cm^3 and (b) $\rho = 10.0$ g/cm^3.

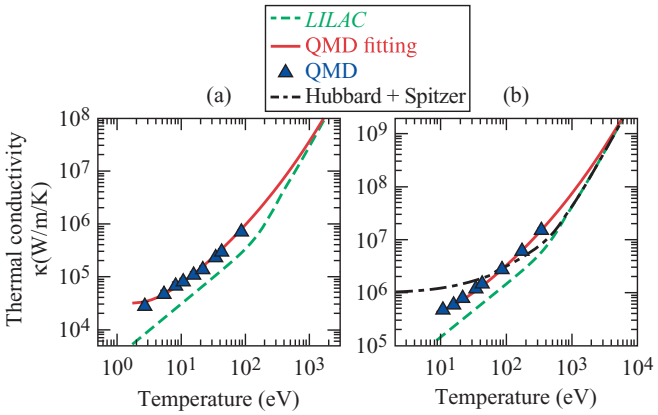

FIG. 5. (Color online) The thermal conductivities from first-principles QMD calculations, the QMD-fitting formula [Eq. (10)], and the hybrid model used in LILAC are plotted as a function of temperature for different deuterium densities of (a) $\rho = 43.105$ g/cm^3 and (b) $\rho = 199.561$ g/cm^3. The Hubbard + Spitzer interpolation results are also depicted by the black dash-dotted line in (b).

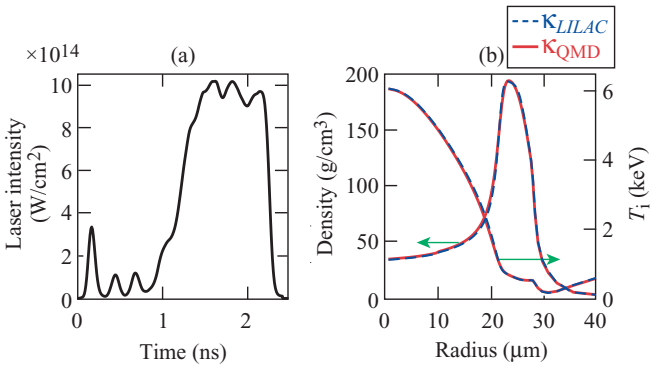

FIG. 6. (Color online) (a) The laser pulse shape used for a high-adiabat ($\alpha = 4$) cryogenic-DT implosion on OMEGA (the $\phi = 868.8$-μm capsule consists of 47 μm of DT ice with an 8.4-μm-thick plastic ablator); (b) comparisons of the density and ion-temperature profiles at peak compression for the two hydrodynamic runs using κ_{LILAC} (blue dashed lines) and κ_{QMD} (red solid lines), respectively. Very little difference is seen in target performance for the two thermal-conductivity models used for such a high-adiabat implosion.

conductivity currently used in our hydrocode LILAC, while the blue solid triangles represent the QMD results. The red solid line is the QMD fit discussed above. We observe that κ_{QMD} is higher than κ_{LILAC} by a factor of 3 to 10 in the coupled and degenerate regimes ($\Gamma > 1, \theta < 1$). The QMD-fit line merges into κ_{LILAC} at a high-T regime ($T > 10T_F$) as expected. In Fig. 5(b) we also showed the Brysk interpolation result [20] between the Hubbard and the Spitzer models by the dash-dotted line. It is noted that the Hubbard formula taken in the Brysky paper [20] is only valid for a Lorentz gas ($Z \gg 1$) and the analytical approximation of function G_Γ was only given for the less-coupling ($\Gamma < 1$) case. Figure 5(b) indicated that the combined Hubbard + Spitzer result still differs from the QMD results. By interpolating and scaling our results for deuterium to the available hydrogen data published in Refs. [39,41], we found the resulted κ_{QMD} variations are within ~10% from these QMD calculations.

IV. EFFECTS OF κ_{QMD} ON ICF IMPLOSIONS

In general, the accurate knowledge of transport property in warm-dense matter is important not only to inertial-confinement fusion, but also to many other fields such as astrophysics, geophysics, and planetary sciences. For example, the thermal conductivity of hydrogen could determine the temperature profiles during the core formation of a giant planet like Jupiter. In this section we exemplify the importance of accurate κ_{QMD} by applying it to the field of ICF. To test how the QMD predicted thermal conductivity of DT affects ICF implosions, we have incorporated the κ_{QMD} fit into our one-dimensional radiation hydrocode LILAC. The hydrodynamics simulations employed the flux-limited thermal conduction model [61–64] with a flux limiter of $f = 0.06$. Two cryogenic DT-target implosions on OMEGA and three NIF direct-drive designs have been examined. These ICF implosions span a wide range of implosion velocities and adiabats. The quantity of adiabat (α) characterizes the plasma degeneracy degree of the imploding DT shell. The lower the adiabat, the more degenerate the DT plasma.

First, we show simulations of the two cryo-DT implosions on OMEGA in Figs. 6 and 7. The typical OMEGA cryo-DT target has a diameter of ~860 μm, which consists of a plastic ablator with a thickness of 8 to 11 μm and a layer

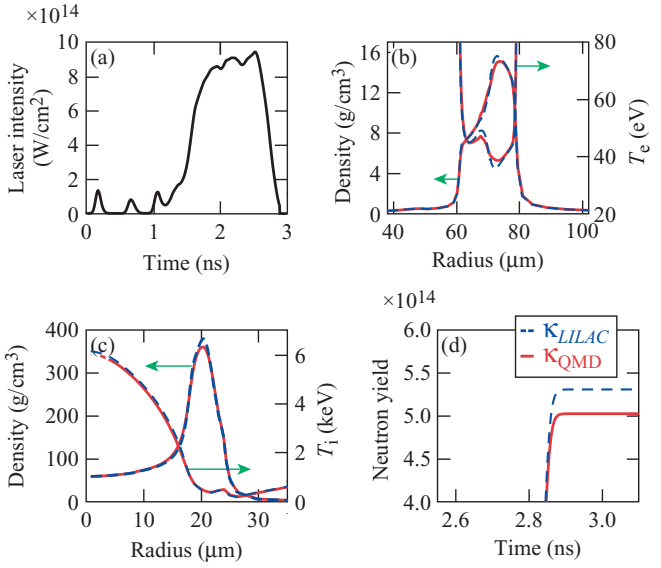

FIG. 7. (Color online) (a) The laser pulse shape used for a low-adiabat ($\alpha = 2.2$) cryogenic-DT implosion on OMEGA (the $\phi = 860.6$-μm capsule consists of 49 μm of DT ice with an 8.3-μm-thick plastic ablator). (b) and (c) Comparisons of the density and temperature profiles at the beginning of deceleration phase and at the peak compression, respectively, for the two hydrodynamic simulations using κ_{LILAC} (blue dashed lines) and κ_{QMD} (red solid lines). (d) The neutron yields as a function of time are plotted for the two cases. A modest variation (~6%) in target performance is seen in such low-adiabat OMEGA implosions, when κ_{QMD} is compared to the hybrid LILAC model.

TABLE II. Comparison of an OMEGA implosion ($\alpha \simeq 2.2$) predicted using $\kappa_{\rm QMD}$ versus $\kappa_{\rm LILAC}$.

	$\kappa_{\rm LILAC}$	$\kappa_{\rm QMD}$
$\langle \rho R \rangle_n$	298 mg/cm^2	296 mg/cm^2
$\langle T_{\rm i} \rangle_n$	4.66 keV	4.64 keV
$\langle P \rangle_n$	197 Gbars	194 Gbars
$\langle \rho \rangle_{\rm peak}$	380.8 g/cm^3	361.7 g/cm^3
Yield	5.34×10^{14}	5.05×10^{14}

of 45 to 65 μm DT ice. In Fig. 6(a), the laser pulse has a relatively high first picket, which sets up the DT shell in a high adiabat of $\alpha \simeq 4$. The density and ion temperature profiles at the peak compression are plotted in Fig. 6(b). The blue dashed line represents the case of using standard $\kappa_{\rm LILAC}$ in the simulation, while the red solid line represents the $\kappa_{\rm QMD}$ simulation. Figure 6(b) shows that there is little change in the target performance for this high-adibat implosion. At the end, the neutron yields are predicted to be 3.32×10^{14} ($\kappa_{\rm LILAC}$) and 3.24×10^{14} ($\kappa_{\rm QMD}$) for the two cases.

Predictions for the low-adiabat ($\alpha \simeq 2.2$) implosion are shown in Fig. 7. Figure 7(a) plots the laser pulse used for this OMEGA implosion. The in-flight plasma conditions are illustrated in Fig. 7(b) at $t = 2.7$ ns, just before stagnation, in which the mass density and electron temperature are drawn as a function of the target radius. Noticeable differences in electron-temperature profiles are seen for the two cases using $\kappa_{\rm QMD}$ and $\kappa_{\rm LILAC}$; the peak density changed slightly when $\kappa_{\rm QMD}$ was used. These differences can affect the target performance at stagnation ($t = 2.84$ ns), as shown by Fig. 7(c). Finally, Fig. 7(d) indicates that the neutron yield is about ~6% lower in the $\kappa_{\rm QMD}$ simulation than for $\kappa_{\rm LILAC}$. Table II summarizes the comparison of other quantities for the two simulations. The neutron-averaged compression ρR and $T_{\rm i}$ are hardly changed, but the peak density and neutron yield vary by ~6%.

Next we discuss the $\kappa_{\rm QMD}$ effects on three different direct-drive–ignition designs for the NIF. These NIF designs have slightly different target sizes varying from $\phi = 3294$ μm to $\phi = 3460$ μm. The thickness of DT-ice layer changes from $d = 125$ μm to $d = 220$ μm; all targets have a plastic ablator at somewhat different thicknesses of 22 to 30 μm. We discuss the $\kappa_{\rm QMD}$ effects on the performance of three NIF designs from a mid-adiabat ($\alpha = 3.2$) implosion to a very-low adiabat ($\alpha = 1.7$) design. Figure 8 shows first the mid-adiabat ($\alpha = 3.2$) design: (a) the triple-picket pulse shape (total energy of 1.5 MJ) and (b) the density and ion-temperature profiles at the bang time ($t = 13.78$ ns, i.e., the time for peak neutron production). Similar to what was seen in Fig. 6, only small differences between $\kappa_{\rm QMD}$ and $\kappa_{\rm LILAC}$ simulations are observed for this mid-adiabat NIF design. The comparison of target performance is summarized in Table III, in which the differences in neutron-averaged ρR, $T_{\rm i}$, pressure $\langle P \rangle_n$, hot-spot radius $R_{\rm hs}$, the hot-spot convergence ratio $C_{\rm hs}$, neutron yield, and gain are all within ~2%.

Figure 9 illustrates the simulation results for a slightly lower adiabat ($\alpha \simeq 2.5$), high-convergence NIF design. Similar to Fig. 7 for the $\alpha = 2.2$ OMEGA implosion, Figs. 9(a)–9(d) plot the pulse shape (total energy of 1.6 MJ), the in-flight

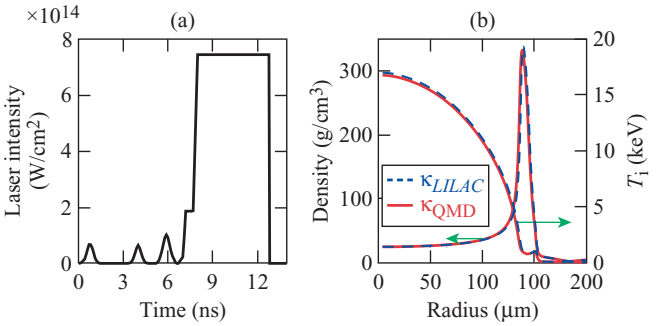

FIG. 8. (Color online) Similar to Fig. 6 but for a NIF-scale implosion: (a) The laser pulse shape for a mid-adiabat ($\alpha = 3.2$), 1.5-MJ direct-drive NIF design (the $\phi = 3460$-μm capsule consists of 220 μm of DT ice with a 30-μm-thick plastic ablator); (b) comparisons of the density and ion-temperature profiles at the peak compression for the two hydrodynamic runs using $\kappa_{\rm LILAC}$ (blue dashed lines) and $\kappa_{\rm QMD}$ (red solid lines), respectively. The effects of using different κ are small for such mid-adiabat designs.

density and electron-temperature profiles at $t = 8.6$ ns, the bang-time density and ion-temperature profiles at $t = 8.91$ ns, and the final neutron yield, respectively. Again, some noticeable differences in the electron temperature at the back surface of the shell can be seen in Fig. 9(b). The observables predicted by the two hydrosimulations using $\kappa_{\rm QMD}$ in contrast to $\kappa_{\rm LILAC}$ are summarized in Table IV. Overall, a level of ~6% increase in target performance is seen in the $\kappa_{\rm QMD}$ simulation when compared to the standard $\kappa_{\rm LILAC}$ case.

We further analyze the implosion dynamics of the NIF design shown in Fig. 9. The noticeable $\rho/T_{\rm e}$ differences at the back of the shell illustrated by Fig. 9(b) must come from the different shock dynamics in early stages of the implosion. To further explore the differences, we have plotted in Fig. 10 the DT-plasma conditions at the shock transit stage. In Fig. 10(a) the density and temperature profiles are displayed for a snapshot at $t = 4.0$ ns. In order to clearly see the differences, we have plotted these profiles as a function of the simulation Lagrangian cell number. At this snapshot, the first shock has propagated to near the back surface (at the 150th cell) of the DT-ice layer. An interesting difference between two simulations can be clearly seen at the first shock front (near the 165th cell), in which the temperature front (at the 175th cell) predicted by the $\kappa_{\rm LILAC}$ simulation does *not*

TABLE III. Comparison of a mid-adiabat ($\alpha = 3.2$) NIF design simulated with $\kappa_{\rm QMD}$ versus $\kappa_{\rm LILAC}$.

	$\kappa_{\rm LILAC}$	$\kappa_{\rm QMD}$
$\langle \rho R \rangle_n$	0.654 g/cm^2	0.655 g/cm^2
$\langle T_{\rm i} \rangle_n$	12.2 keV	12.1 keV
$\langle P \rangle_n$	250 Gbars	248 Gbars
$\langle \rho \rangle_{\rm peak}$	337.4 g/cm^3	331.8 g/cm^3
$R_{\rm hs}$	91.4 μm	91.3 μm
$C_{\rm hs}$	18.9	18.9
Yield	6.45×10^{18}	6.33×10^{18}
Gain	12.1	11.8

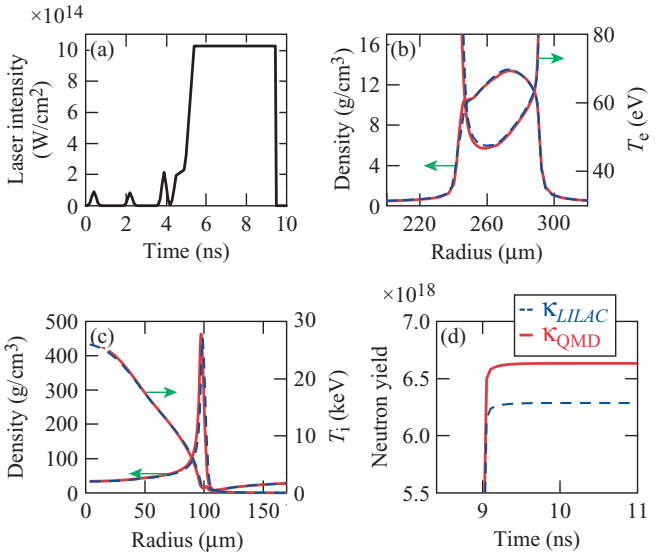

FIG. 9. (Color online) Tests on a high-implosion-velocity NIF design: (a) The laser pulse shape ($\alpha = 2.5$) has a total 1.6-MJ energy (the $\phi = 3294$-μm capsule consists of 125 μm of DT ice with a 22-μm-thick plastic ablator). (b) and (c) Comparison of the density and temperature profiles at the beginning of the deceleration phase and at peak compression, respectively, for the two hydrodynamic simulations using $\kappa_{\rm LILAC}$ (blue dashed lines) and $\kappa_{\rm QMD}$ (red solid lines). The neutron yields as a function of time are plotted in (d) for the two cases. The use of $\kappa_{\rm QMD}$ changes the one-dimensional (1D) prediction of implosion performance modestly (~6%).

follow the density front of the shock. This occurs because the standard $\kappa_{\rm LILAC}$ significantly underestimates the thermal conductivity by an order of magnitude, for the shocked-DT plasma condition of $\rho_{\rm DT} \simeq 1.0$ g/cm^2 and $T_{\rm e} \simeq 1$ to 2 eV. The reduced thermal conductivity in $\kappa_{\rm LILAC}$ decreases the heat flow behind the shock front. On the contrary, the $\kappa_{\rm QMD}$ simulation (red solid lines) indicates the same shock-front location for both density and temperature, as they should be. Differences in both density and temperature are also seen after the second shock [near the 260th cell shown in Fig. 10(a)]. The $\kappa_{\rm LILAC}$ simulation predicts more "artificial" fluctuations in density and temperature after the second shock. Figure 10(b) shows another snapshot at $t = 4.8$ ns, when the first shock breaks out at the back of the DT-ice layer into the DT gas. A large

TABLE IV. Comparison of a low-adiabat ($\alpha = 2.5$) NIF design simulated with $\kappa_{\rm QMD}$ versus $\kappa_{\rm LILAC}$.

	$\kappa_{\rm LILAC}$	$\kappa_{\rm QMD}$
$\langle \rho R \rangle_n$	0.646 g/cm^2	0.661 g/cm^2
$\langle T_{\rm i} \rangle_n$	20.8 keV	21.5 keV
$\langle P \rangle_n$	715 Gbars	763 Gbars
$\langle \rho \rangle_{\rm peak}$	456.8 g/cm^3	466.9 g/cm^3
$R_{\rm hs}$	56.2 μm	53.8 μm
$C_{\rm hs}$	29.3	30.6
Yield	6.3×10^{18}	6.7×10^{18}
Gain	11.1	11.7

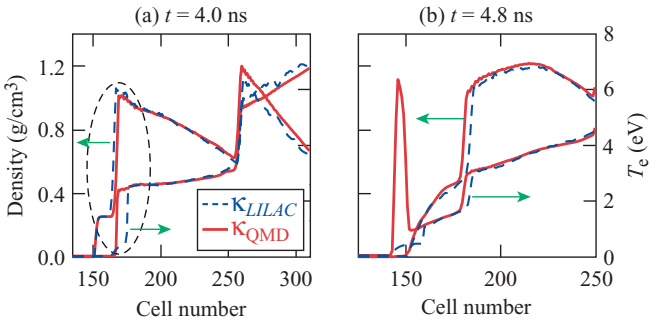

FIG. 10. (Color online) The predicted shock conditions during the shock transit stage in the DT ice, for the NIF design plotted in Fig. 9. The density and electron temperature are plotted as a function of the Lagrangian cell numbers for times at (a) $t = 4.0$ ns and (b) $t = 4.8$ ns. Again, the two cases of using $\kappa_{\rm LILAC}$ (blue dashed lines) and $\kappa_{\rm QMD}$ (red solid lines) are compared.

difference in electron-temperature profile is observed for the two simulations: The instant heat conduction in the $\kappa_{\rm QMD}$ case results in the immediate heating up of the releasing back surface, which is in contrast to the delayed heating in the $\kappa_{\rm LILAC}$ simulation. These different shock dynamics at the early stage of implosion cause the observable density-temperature variations late in the implosion, plotted in Fig. 9(b). This is the major contribution responsible for the final difference in target performance, which is discussed below.

Finally, the very low adiabat ($\alpha \simeq 1.7$) NIF design is examined in Fig. 11 and Table V. The implosion is

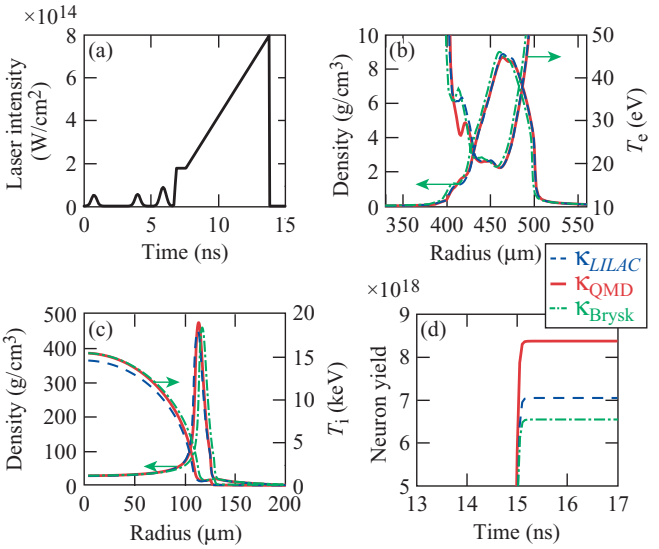

FIG. 11. (Color online) Similar to Fig. 9 but for a relatively lower adiabat ($\alpha = 1.7$) and lower-implosion-velocity ($v_{\rm imp} = 3.3 \times 107$ cm/s) NIF design: (a) The laser pulse shape has a total energy of 1.2 MJ and the $\phi = 3420$-μm capsule consists of 180 μm of DT ice with a 30-μm plastic ablator. (b) and (c) Comparison of the density and temperature profiles at the beginning of the deceleration phase and at the peak compression, respectively. (d) Comparison of the neutron yields for the three cases, which shows about ~20% variation in the 1D predictions of target performance using $\kappa_{\rm LILAC}$ and $\kappa_{\rm Brysk}$ (green dash-dotted lines) in comparison to the $\kappa_{\rm QMD}$ modeling.

TABLE V. Comparison of a very low-adiabat ($\alpha = 1.7$) NIF design simulated with $\kappa_{\rm QMD}$ versus $\kappa_{\rm LILAC}$.

	$\kappa_{\rm LILAC}$	$\kappa_{\rm QMD}$
$\langle \rho R \rangle_n$	0.679 g/cm^2	0.69 g/cm^2
$\langle T_{\rm i} \rangle_n$	13.1 keV	14.1 keV
$\langle P \rangle_n$	299 Gbars	335 Gbars
$\langle \rho \rangle_{\rm peak}$	475.7 g/cm3	495.1 g/cm^3
$R_{\rm hs}$	80.9 μm	79.3 μm
$C_{\rm hs}$	21.1	21.6
Yield	7.07×10^{18}	8.41×10^{18}
Gain	16.6	19.7

designed to be driven by an 1.2-MJ pulse shape shown in Fig. 11(a), which has a ramping and low-intensity main pulse to avoid possible preheat from two-plasmon-decay–induced hot electrons [65,66]. The implosion velocity for this design is about 3.3×10^7 cm/s. Since the adiabat is so low that the DT-plasma conditions for the in-flight shell lie deeply within the more-degenerate and coupled regime, where $\kappa_{\rm QMD}$ is much higher than $\kappa_{\rm LILAC}$, the effects of using $\kappa_{\rm QMD}$ are dramatically increased when compared to the higher-adiabat implosions discussed above. From Table V and Fig. 11, a level of ~20% variation in target performance (yield and gain) is observed in the predictions of the two cases. Figure 11(b) shows that the simulation using $\kappa_{\rm QMD}$ predicts a lower electron-temperature profile for the back of the shell ($R \simeq 420$ μm). This results in a larger peak density of the shell and higher $T_{\rm i}$ at the bang time for the $\kappa_{\rm QMD}$ case, illustrated by Fig. 11(c), thereby leading to more neutron yields and gain. In addition, we have also compared the simulation result using the Brysk model (green/dash-dotted line) in Figs. 11(b)–11(d). The Brysk model gives slightly different implosion dynamics than the $\kappa_{\rm LILAC}$ modeling; While the final neutron yield from the Brysk model is lower than both $\kappa_{\rm QMD}$ and $\kappa_{\rm LILAC}$ simulations.

To test the conventional speculation that $\kappa_{\rm QMD}$ affects mainly the hot-spot formation, we performed a "hybrid" simulation for this design by switching $\kappa_{\rm QMD}$ to the standard $\kappa_{\rm LILAC}$ during the target deceleration phase and burn ($t > 13.6$ ns). This hybrid simulation gives a total neutron yield of 9.29×10^{18} and a gain of 21.8. Comparing with the full $\kappa_{\rm QMD}$ simulation results ($Y = 8.41 \times 10^{18}$ and $G = 19.7$), the variation is modest with respect to the change from the full $\kappa_{\rm LILAC}$ simulation to the full $\kappa_{\rm QMD}$ case. This indicates that the major part of the $\kappa_{\rm QMD}$ effects on target performance comes from the shock dynamics during the early stage of the implosion, although the use of $\kappa_{\rm QMD}$ moderately decreases the target performance during the hot-spot formation.

V. SUMMARY

For inertial confinement fusion applications, we have figured out a global formula of deuterium thermal conductivity in a wide range of densities and temperatures, using the quantum molecular dynamics simulations. For the density and temperature conditions in an imploding DT shell, the QMD-calculated thermal conductivity $\kappa_{\rm QMD}$ is higher by a factor of 3 to 10 than the hybrid Spitzer-Lee-More model $\kappa_{\rm LILAC}$ currently adopted in our hydrocodes. To test its effects on ICF implosions, we have fitted $\kappa_{\rm QMD}$ to a fifth-order polynomial function of Γ and θ and incorporated this fit into our hydrocodes. The hydrodynamic simulations of both OMEGA cryo-DT implosions and direct-drive NIF designs have been performed using $\kappa_{\rm QMD}$. Compared with the standard simulation results using $\kappa_{\rm LILAC}$, we found the ICF implosion performance predicted by $\kappa_{\rm QMD}$ could vary as high as ~20%. The lower the adiabat of the DT shell, the more the effects of $\kappa_{\rm QMD}$ are observed. Detailed analyses of the implosion dynamics have identified that the shock-dynamics differences at an early stage of the implosion, predicted by $\kappa_{\rm QMD}$ and $\kappa_{\rm LILAC}$, predominantly contribute to the final variations of implosion performance (neutron yield and target gain). This is in contrast to the previous speculation that $\kappa_{\rm QMD}$ might affect ICF mainly during the hot-spot formation. The thermal conductivities of deuterium reported in this paper, together with the established FPEOS tables [11,45] and opacity tables (to be built) from such first-principles calculations, could provide the complete physical information of fusion fuel at high-energy-density conditions for accurate ICF hydrosimulations. The same strategy also applies for building self-consistent tables for ICF-relevant ablator materials. These efforts could increase the predictive capability of hydrodynamic modeling of ICF implosions.

ACKNOWLEDGMENTS

This material is based on work supported by the Department of Energy National Nuclear Security Administration under Award Number DE-NA0001944, the University of Rochester, and the New York State Energy Research and Development Authority. This work was also supported by Scientific Campaign 10 at the Los Alamos National Laboratory, operated by Los Alamos National Security, LLC for the National Nuclear Security Administration of the U.S. Department of Energy under Contract No. DE-AC52-06NA25396. The support of DOE does not constitute an endorsement by DOE of the views expressed in this article. S.X.H. acknowledges the advice from Professor G. Kresse on the Coulombic potential for high-density VASP simulations.

[1] J. Nuckolls, L. Wood, A. Thiessen, and G. Zimmerman, Nature (London) **239**, 139 (1972); S. Atzeni and J. Meyer-ter-Vehn, *The Physics of Inertial Fusion: Beam Plasma Interaction, Hydrodynamics, Hot Dense Matter*, International Series of Monographs on Physics (Clarendon, Oxford, 2004).

[2] J. D. Lindl, Phys. Plasmas **2**, 3933 (1995).

[3] C. Cherfils-Clérouin, C. Boniface, M. Bonnefille, P. Fremerye, D. Galmiche, P. Gauthier, J. Giorla, F. Lambert, S. Laffite, S. Liberatore, P. Loiseau, G. Malinie, L. Masse, P. E. Masson-Laborde, M. C. Monteil, F. Poggi, P. Seytor, F. Wagon, and J. L. Willien, J. Phys.: Conf. Ser. **244**, 022009 (2010).

[4] R. L. McCrory, R. Betti, T. R. Boehly, D. T. Casey, T. J. B. Collins, R. S. Craxton, J. A. Delettrez, D. H. Edgell, R. Epstein, J. A. Frenje, D. H. Froula, M. Gatu-Johnson, V. Y. Glebov, V. N. Goncharov, D. R. Harding, M. Hohenberger, S. X. Hu, I. V. Igumenshchev, T. J. Kessler, J. P. Knauer, C. K. Li, J. A. Marozas, F. J. Marshall, P. W. McKenty, D. D. Meyerhofer, D. T. Michel, J. F. Myatt, P. M. Nilson, S. J. Padalino, R. D. Petrasso, P. B. Radha, S. P. Regan, T. C. Sangster, F. H. Séguin, W. Seka, R. W. Short, A. Shvydky, S. Skupsky, J. M. Soures, C. Stoeckl, W. Theobald, B. Yaakobi, and J. D. Zuegel, Nucl. Fusion **53**, 113021 (2013).

[5] D. D. Meyerhofer, R. L. McCrory, R. Betti, T. R. Boehly, D. T. Casey, T. J. B. Collins, R. S. Craxton, J. A. Delettrez, D. H. Edgell, R. Epstein, K. A. Fletcher, J. A. Frenje, Y. Y. Glebov, V. N. Goncharov, D. R. Harding, S. X. Hu, I. V. Igumenshchev, J. P. Knauer, C. K. Li, J. A. Marozas, F. J. Marshall, P. W. McKenty, P. M. Nilson, S. P. Padalino, R. D. Petrasso, P. B. Radha, S. P. Regan, T. C. Sangster, F. H. Séguin, W. Seka, R. W. Short, D. Shvarts, S. Skupsky, J. M. Soures, C. Stoeckl, W. Theobald, and B. Yaakobi, Nucl. Fusion **51**, 053010 (2011).

[6] V. N. Goncharov, T. C. Sangster, T. R. Boehly, S. X. Hu, I. V. Igumenshchev, F. J. Marshall, R. L. McCrory, D. D. Meyerhofer, P. B. Radha, W. Seka, S. Skupsky, C. Stoeckl, D. T. Casey, J. A. Frenje, and R. D. Petrasso, Phys. Rev. Lett. **104**, 165001 (2010).

[7] M. C. Herrmann, M. Tabak, and J. D. Lindl, Nucl. Fusion **41**, 99 (2001).

[8] C. D. Zhou and R. Betti, Phys. Plasmas **15**, 102707 (2008).

[9] S. X. Hu, V. A. Smalyuk, V. N. Goncharov, J. P. Knauer, P. B. Radha, I. V. Igumenshchev, J. A. Marozas, C. Stoeckl, B. Yaakobi, D. Shvarts, T. C. Sangster, P. W. McKenty, D. D. Meyerhofer, S. Skupsky, and R. L. McCrory, Phys. Rev. Lett. **100**, 185003 (2008).

[10] J. Clérouin and J.-F. Dufrêche, Phys. Rev. E **64**, 066406 (2001); L. Caillabet, S. Mazevet, and P. Loubeyre, Phys. Rev. B **83**, 094101 (2011).

[11] S. X. Hu, B. Militzer, V. N. Goncharov, and S. Skupsky, Phys. Rev. B **84**, 224109 (2011).

[12] M. A. Morales, L. X. Benedict, D. S. Clark, E. Schwegler, I. Tamblyn, S. A. Bonev, A. A. Correa, and S. W. Haan, High Energy Density Phys. **8**, 5 (2012).

[13] S. Hamel, L. X. Benedict, P. M. Celliers, M. A. Barrios, T. R. Boehly, G. W. Collins, T. Döppner, J. H. Eggert, D. R. Farley, D. G. Hicks, J. L. Kline, A. Lazicki, S. LePape, A. J. Mackinnon, J. D. Moody, H. F. Robey, E. Schwegler, and P. A. Sterne, Phys. Rev. B **86**, 094113 (2012); P. Loubeyre, S. Brygoo, J. Eggert, P. M. Celliers, D. K. Spaulding, J. R. Rygg, T. R. Boehly, G. W. Collins, and R. Jeanloz, *ibid.* **86**, 144115 (2012).

[14] J. Vorberger, D. O. Gericke, and W. D. Kraeft, High Energy Density Phys. **9**, 448 (2013).

[15] C. Wang and P. Zhang, Phys. Plasmas **20**, 092703 (2013).

[16] V. V. Karasiev, D. P. Chakraborty, O. A. Shukruto, and S. B. Trickey, Phys. Rev. B **88**, 161108 (2013).

[17] B. Militzer and D. M. Ceperley, Phys. Rev. Lett. **85**, 1890 (2000); B. Militzer, D. M. Ceperley, J. D. Kress, J. D. Johnson, L. A. Collins, and S. Mazevet, *ibid.* **87**, 275502 (2001).

[18] J. M. McMahon, M. A. Morales, C. Pierleoni, and D. M. Ceperley, Rev. Mod. Phys. **84**, 1607 (2012).

[19] L. Collins, I. Kwon, J. Kress, N. Troullier, and D. Lynch, Phys. Rev. E **52**, 6202 (1995).

[20] H. Brysk, P. M. Campbell, and P. Hammerling, Plasma Phys. **17**, 473 (1975).

[21] L. Spitzer, Jr. and R. Härm, Phys. Rev. **89**, 977 (1953).

[22] J. Daligault and G. Dimonte, Phys. Rev. E **79**, 056403 (2009).

[23] L. X. Benedict, J. N. Glosli, D. F. Richards, F. H. Streitz, S. P. Hau-Riege, R. A. London, F. R. Graziani, M. S. Murillo, and J. F. Benage, Phys. Rev. Lett. **102**, 205004 (2009).

[24] B. Xu and S. X. Hu, Phys. Rev. E **84**, 016408 (2011).

[25] L. X. Benedict, M. P. Surh, J. I. Castor, S. A. Khairallah, H. D. Whitley, D. F. Richards, J. N. Glosli, M. S. Murillo, C. R. Scullard, P. E. Grabowski, D. Michta, and F. R. Graziani, Phys. Rev. E **86**, 046406 (2012).

[26] C. Blancard, J. Clérouin, and G. Faussurier, High Energy Density Phys. **9**, 247 (2013).

[27] W. B. Hubbard, Astrophys. J. **146**, 858 (1966).

[28] Y. T. Lee and R. M. More, Phys. Fluids **27**, 1273 (1984).

[29] S. Ichimaru and S. Tanaka, Phys. Rev. A **32**, 1790 (1985); H. Kitamura and S. Ichimaru, Phys. Rev. E **51**, 6004 (1995).

[30] D. A. Liberman, Phys. Rev. B **20**, 4981 (1979).

[31] B. Wilson, V. Sonnad, P. Sterne, and W. Isaacs, J. Quant. Spectrosc. Radiat. Transfer **99**, 658 (2006).

[32] G. Faussurier, C. Blancard, P. Cossé, and P. Renaudin, Phys. Plasmas **17**, 052707 (2010); J. Clérouin, C. Starrett, G. Faussurier, C. Blancard, P. Noiret, and P. Renaudin, Phys. Rev. E **82**, 046402 (2010).

[33] J. G. Clérouin and S. Bernard, Phys. Rev. E **56**, 3534 (1997).

[34] L. A. Collins, S. R. Bickham, J. D. Kress, S. Mazevet, T. J. Lenosky, N. J. Troullier, and W. Windl, Phys. Rev. B **63**, 184110 (2001).

[35] M. P. Desjarlais, Phys. Rev. B **68**, 064204 (2003).

[36] S. A. Bonev, B. Militzer, and G. Galli, Phys. Rev. B **69**, 014101 (2004).

[37] J. D. Kress, J. S. Cohen, D. A. Horner, F. Lambert, and L. A. Collins, Phys. Rev. E **82**, 036404 (2010).

[38] V. Recoules, F. Lambert, A. Decoster, B. Canaud, and J. Clérouin, Phys. Rev. Lett. **102**, 075002 (2009).

[39] F. Lambert, V. Recoules, A. Decoster, J. Clérouin, and M. Desjarlais, Phys. Plasmas **18**, 056306 (2011).

[40] D. E. Hanson, L. A. Collins, J. D. Kress, and M. P. Desjarlais, Phys. Plasmas **18**, 082704 (2011).

[41] B. Holst, M. French, and R. Redmer, Phys. Rev. B **83**, 235120 (2011).

[42] C. E. Starrett, J. Clérouin, V. Recoules, J. D. Kress, L. A. Collins, and D. E. Hanson, Phys. Plasmas **19**, 102709 (2012).

[43] C. Wang, Y. Long, X.-T. He, J.-F. Wu, W.-H. Ye, and P. Zhang, Phys. Rev. E **88**, 013106 (2013).

[44] For details of the ABINIT code, please refer to http://www.abinit.org/.

[45] S. X. Hu, B. Militzer, V. N. Goncharov, and S. Skupsky, Phys. Rev. Lett. **104**, 235003 (2010).

[46] R. Kubo, J. Phys. Soc. Jpn. **12**, 570 (1957); D. A. Greenwood, Proc. Phys. Soc. London **71**, 585 (1958).

[47] J. Delettrez, R. Epstein, M. C. Richardson, P. A. Jaanimagi, and B. L. Henke, Phys. Rev. A **36**, 3926 (1987).

[48] I. Kwon, J. D. Kress, and L. A. Collins, Phys. Rev. B **50**, 9118 (1994).

[49] M. P. Desjarlais, J. D. Kress, and L. A. Collins, Phys. Rev. E **66**, 025401 (2002).

[50] B. Holst, R. Redmer, and M. P. Desjarlais, Phys. Rev. B **77**, 184201 (2008).
[51] G. Kresse and J. Hafner, Phys. Rev. B **47**, 558 (1993).
[52] G. Kresse and J. Hafner, Phys. Rev. B **49**, 14251 (1994); G. Kresse and J. Furthmüller, *ibid.* **54**, 11169 (1996).
[53] J. P. Perdew, K. Burke, and M. Ernzerhof, Phys. Rev. Lett. **77**, 3865 (1996); **78**, 1396(E) (1997).
[54] G. Kresse (private communication, 2013).
[55] P. M. Celliers, G. W. Collins, L. B. Da Silva, D. M. Gold, R. Cauble, R. J. Wallace, M. E. Foord, and B. A. Hammel, Phys. Rev. Lett. **84**, 5564 (2000).
[56] T. R. Boehly, D. H. Munro, P. M. Celliers, R. E. Olson, D. G. Hicks, V. N. Goncharov, G. W. Collins, H. F. Robey, S. X. Hu, J. A. Marozas, T. C. Sangster, O. L. Landen, and D. D. Meyerhofer, Phys. Plasmas **16**, 056302 (2009).
[57] T. R. Boehly, V. N. Goncharov, W. Seka, S. X. Hu, J. A. Marozas, D. D. Meyerhofer, P. M. Celliers, D. G. Hicks, M. A. Barrios, D. Fratanduono, and G. W. Collins, Phys. Plasmas **18**, 092706 (2011).
[58] T. R. Boehly, V. N. Goncharov, W. Seka, M. A. Barrios, P. M. Celliers, D. G. Hicks, G. W. Collins, S. X. Hu, J. A. Marozas, and D. D. Meyerhofer, Phys. Rev. Lett. **106**, 195005 (2011).
[59] L. A. Collins, J. D. Kress, and D. E. Hanson, Phys. Rev. B **85**, 233101 (2012).
[60] See Supplemental Material at http://link.aps.org/supplemental/10.1103/PhysRevE.89.043105 for the tabulated thermal conductivity of deuterium.
[61] R. C. Malone, R. L. McCrory, and R. L. Morse, Phys. Rev. Lett. **34**, 721 (1975).
[62] S. X. Hu, V. A. Smalyuk, V. N. Goncharov, S. Skupsky, T. C. Sangster, D. D. Meyerhofer, and D. Shvarts, Phys. Rev. Lett. **101**, 055002 (2008).
[63] S. X. Hu, P. B. Radha, J. A. Marozas, R. Betti, T. J. B. Collins, R. S. Craxton, J. A. Delettrez, D. H. Edgell, R. Epstein, V. N. Goncharov, I. V. Igumenshchev, F. J. Marshall, R. L. McCrory, D. D. Meyerhofer, S. P. Regan, T. C. Sangster, S. Skupsky, V. A. Smalyuk, Y. Elbaz, and D. Shvarts, Phys. Plasmas **16**, 112706 (2009).
[64] S. X. Hu, V. N. Goncharov, P. B. Radha, J. A. Marozas, S. Skupsky, T. R. Boehly, T. C. Sangster, D. D. Meyerhofer, and R. L. McCrory, Phys. Plasmas **17**, 102706 (2010).
[65] D. H. Froula, B. Yaakobi, S. X. Hu, P.-Y. Chang, R. S. Craxton, D. H. Edgell, R. Follett, D. T. Michel, J. F. Myatt, W. Seka, R. W. Short, A. Solodov, and C. Stoeckl, Phys. Rev. Lett. **108**, 165003 (2012).
[66] S. X. Hu, D. T. Michel, D. H. Edgell, D. H. Froula, R. K. Follett, V. N. Goncharov, J. F. Myatt, S. Skupsky, and B. Yaakobi, Phys. Plasmas **20**, 032704 (2013).